

Switching based Spin Transfer Torque Oscillator with zero-bias field and large tuning-ratio

Gaurav Gupta[†], Zhifeng Zhu and Gengchiau Liang^{}*

Department of Electrical and Computer Engineering, National University of Singapore,
Singapore 117576

We propose a novel concept of obtaining oscillations with frequencies in very-high frequency (VHF) and ultra-high frequency (UHF) bands. A traditional spin torque nano-oscillator (STNO) has one or a set of pinned layers (PL) and one or more a set of locked free layers (FL) which precesses in a fixed orbit, defined by a precession angle, which results in magneto-resistance (MR) oscillations. In STNO, with aligned or even orthogonal easy-axis of the magnetic layers and with or without external bias magnetic field, it is not possible to attain full MR swing. The constricted MR swing jeopardizes the extracted output power. Furthermore, the orbit is strongly afflicted with thermal fluctuations or magnetic noise. In stark contrast to the operation principle of STNO, we theoretically demonstrate, with the practical parameters from the experiments, that with a unidirectional current in a dual asymmetric free-layers (with no pinned layer) based perpendicular magnetic tunnel junction (pMTJ) both the free layers can attain complete and out-of-phase self-sustained switching without the aid of any external field. This design enables full MR swing, and hence larger output power, for stable and more thermally robust free-running oscillations. Furthermore, the integration with the n-type metal-oxide-semiconductor (NMOS) field-effect transistors at 130, 65 and 14 nm node is appraised to expound its effect on the oscillator performance, controllability with DC bias and the design constraints, to demonstrate the viability of the design as a dynamically controllable oscillator for practical on-chip implementation.

I. INTRODUCTION

On-chip oscillators [1] generate stable periodic oscillations, whose voltage (VCO), current (CCO) or digital (DCO) control serves as an integral component of the phase-locked loop (PLL) and radio-frequency (RF) transceivers. PLL generates the clock signal for the chip serving as its heart, where it can either output the same or multiply or divide the VCO frequency to suit the application. Frequency (f) control of the oscillators enables dynamic-frequency-scaling (DFS) scheme [2] for optimizing the low-power modes. Furthermore, as the indispensable blocks in RF transceiver circuits, oscillators are used for modulation and clock recovery. For these applications, an ideal oscillator needs large quality factor (Q) (i.e. small phase noise), low power consumption (P_{IN}), large output power or voltage swing (P_O or V_O), integrability with CMOS, large tunability ratio (f_{max}/f_{min}) and small die area occupancy in the desired frequency regime. Extant solutions [1, 3] are based on the ring-oscillators, which have low Q , for sub-GHz and LC-tank oscillators (large Q) for a few GHz range, because phase noise for the ring oscillators further degrades as the frequency is scaled-up. Furthermore, LC oscillators have small tuning range [1, 4], have large P_{IN} , are difficult to integrate in the very-large scale integration (VLSI) chips and occupy large area because of the large inductor and varactor size even in low GHz regime at which custom-designed chips can operate.

To overcome these issues, recently spin-torque nano-oscillators (STNOs) and spin-hall nano-oscillators (SHNO) have been proposed [5] and integrated with CMOS [6]. They are expected to consume small area (\sim area of magnetic-tunnel junction (MTJ)), less power and provide ultra-wide-band operation [7, 8]. STNOs are based on the precession of a free-layer (or set of locked [9-11] FLs) of MTJ in a fixed orbit determined by the precessional angle [5], with a single or a set of fixed reference/pinned layer [12]. This precession in a locked orbit results in an oscillatory change in the magnetization of the free layer (s) with respect to

that of the reference layer, which translates into a resistance change of a MTJ (or spin-valve in case of metallic spacer), R_{MTJ} and thus an output voltage swing. To increase the output voltage swing by increasing the observable fraction of the MR in the oscillations, the combination of multiple in-plane and perpendicular magnetization free and pinned/reference layers (orthogonal set of layers [10, 13]) in a MTJ has also been promulgated for a very large precession angle. It enables near full rotation of one of the free layers, without external bias magnetic-field H_{Applied} , as an improvement over an all in-plane or all-perpendicular designs which need H_{Applied} . However, the use of orthogonal layers across the spacer (metal like Cu or insulator like MgO) inherently limits the MR of these stacks. Furthermore recently, locked precessional orbits of dual free layer designs, without polarizing layer, for in-plane magnetization (ii-MTJ) and with assistance of H_{Applied} have also been shown to produce stable oscillatory output [14, 15]. Without H_{Applied} , the output signal has been shown to be very weak (< -100 dBm) [16]. Moreover, for multiple precessional orbits with the MR and the resistance oscillations depending on the dynamic angle of the precessions, the effect of the magnetic noise becomes stronger in this design compared to traditional STNO. Furthermore, sophisticated designs with tilted anisotropy, operating without H_{Applied} , with weak output (< -65 dBm) [17], and more recently with large P_{O} (nearly -26 dBm at 6.7mA current bias) which need very precise control of H_{Applied} and especially designed microstructure for the magnet [18, 19] in sombrero-shaped MTJ, have been demonstrated. As a consequence of the reliance on the fixed precessional orbit, the magnetic noise resulting from the thermal fluctuations strongly affects the performance of a STNO (for instance see Fig. 1 of Ref. [20] or Fig. 5 of Ref. [21]), by randomizing the phase of the precession. This especially becomes pernicious when MTJ area is down-scaled because the thermal field scales as an inverse root of the magnet volume. These issues greatly limit its applicability in the real applications [7].

Therefore, in this work we propose a simple design of a spintronic oscillator, with no exotic structure or tilted anisotropy constraints, as conceptually illustrated in Fig. 1. The generated oscillations (85-1002 MHz) are in VHF (30-300 MHz) and UHF (300-1000 MHz) frequency bands [22] which more generally serve application-specific integrated circuits (ASICs) [2, 23-27]. Furthermore, this frequency range also serves the RF band for LoRa protocol (868 MHz for Europe, 915 MHz for North America and 430 MHz for Asia) [28-30] deployed for low-cost bi-directional secure low-power wide-area-network (LPWAN) wireless communication channel in internet-of-things (IoT), machine-to-machine (M2M), smart city and industrial applications [31]. This is in contrast to STNO which is normally over this range and gets to tens of GHz and thus applied as microwave source/detector and in wireless transceivers [5, 7] for other protocols like Bluetooth and Wi-Fi. The proposed design is based on dual asymmetric free-layers, with no pinned layer, in a perpendicular magnetic tunnel junction (pMTJ) and operates without any bias magnetic field. The design has large tunability ratio and can deliver relatively large output power because MR oscillations attain full theoretical maximum, which in turn would also be much larger than MTJs with magnetic layers with orthogonal easy-axis. To achieve this, the design deploys a different operation principle than STNO. It is based on the switching of both the free-layers with unidirectional current in pMTJ structure, where one of the free-layer would have traditionally served as a reference layer and mandated current reversal for switching-back the traditional free-layer. It is shown that both layers can attain complete and out-of-phase self-sustained switching with a DC electrical bias to produce oscillations which are more thermally robust than for STNO.

The frequency is shown to scale directly with the MTJ current I_{MTJ} . In CCO configuration, the design has tunability of over a decade. This is much superior to STNO [32] and ring oscillators [33] for which even attaining an octave (electronic control for STNO) is a challenge, and thus proposed design is better suited for DFS schemes. Since, CCO would

warrant implementation of the stable current sources/mirrors over a wide operating range, which would heavily penalize the design in terms of power and area, simply driving the MTJ with a NMOS in VCO configuration is also appraised. Therefore, as illustrated in Fig. 2(a), the impact of integration and the control of the oscillator via foundry calibrated NMOS is also examined across the complementary metal–oxide–semiconductor (CMOS) nodes (130, 65 and 14 nm) by tuning either the gate voltage V_{GS} (suggested method in this work) or the node voltage V_{DD} (akin to the ring oscillator based VCOs) of the cell, where cell is referred to a system of a MTJ with a (or set of) driving transistors. It is shown that transistor has significant impact on the performance metrics of the oscillator. The performance in general degrades, yet is shown to be better than traditional STNOs in the CCO configuration. Furthermore, we show that the NMOS area dominates the cell-size instead of the MTJ area, and hence, should be the one compared with the traditional ring or LC oscillators to claim the area benefits. Moreover, a larger node because of its larger supply voltage has better current drive and thus an iso-frequency comparison exhibits smaller channel area and larger output power for a larger node.

The article is organized as follows. In Sec. II, the methodology of our theoretical simulation of the proposed design is explained. Sec. III discusses the results and is anatomized into four sub-sections. In sub-section III.A, the operation principle and the device physics is expounded, the effect of thermal fluctuation i.e. magnetic noise is considered in III.B. Results for the design driven by a current-source thus operating it in CCO configuration is presented in III.C, while integration of transistors to operate in VCO configuration is assayed in III.D. This is followed in Sec. IV with the summary and conclusions of our study.

II. METHODOLOGY

The simulation framework illustrated in Fig. 2(b) expounds all mechanisms considered in this work, and the flow of variables across the framework. Two methods are considered in this work to drive unidirectional current through a pMTJ based proposed oscillator. The first one is constant current source (akin to suggested for STNO) which operates the device in the CCO configuration (Fig. 1), and corresponds to only the MTJ dynamics in the framework. The second one is NMOS with MTJ on the drain end of the transistor whose supply node V_{DD} (akin to ring-oscillators) or gate (suggested method for this design) is controlled via input DC voltage, which operates the design in the VCO configuration (Fig. 2(a)). This invokes the full framework shown in Fig. 2(b). Other configurations, like MTJ on the source end or use of the MOS in the diode mode results in inferior performance of the oscillator and thus not shown here.

The magnetization dynamics is solved via coupled Landau–Lifshitz–Gilbert (LLG) equation, integrated via fourth order Runge-Kutta method [34], for two FLs with macrospin model which has been shown to be valid for dimensions considered in this work [35-37]. The problem is numerically solved in matlab which is dynamically coupled with SMASH to solve at every time-interval Δt of 5 ps for an updated angle between the two magnetization vectors and the voltage across the MTJ. Unless stated otherwise, the oscillator characteristics are extracted for 10 μ s run which results in two-million sampling points of the data which is subsequently parsed by Fast-Fourier Transform (FFT) to extract oscillator characteristics like fundamental frequency, linewidth, quality factor and output voltage swing V_O . The output power P_O in dBm is computed as $10 + 20 \log_{10}(V_O)$. For input-power P_{IN} and area, in CCO configuration only MTJ is considered (akin to the STNO literature) while in VCO configuration both MTJ and transistor are accounted. Next, the Resistance-Area product or $RA = 4.7 \Omega\text{-}\mu\text{m}^2$ is taken from CoFeB pMTJ from imec [38] with zero-bias TMR (Tunneling

Magnetoresistance) i.e. $\text{TMR}_0 = 143\%$ and MgO thickness $t_{\text{MgO}} = 1$ nm. Throughout the text, MTJ dimensions (in nm) along x, y and z axis are respectively expressed as: length \times width \times thickness_{FL₁} (thickness_{FL₂}), with default value of 50nm \times 50nm \times 1.6nm(1.2nm). Both damping and field-like torque (DLT and FLT), a_{\parallel} and a_{\perp} respectively, are considered in the coupled LLG equation as [39],

$$\left(\frac{1+\alpha^2}{\gamma}\right)\frac{d\mathbf{M}_i}{dt} = -\mathbf{M}_i \times \left[\mathbf{B}_{\text{Eff}}^i - (a_{\perp}^i + \alpha a_{\parallel}^i)\mathbf{p}_j\right] - \frac{\mathbf{M}_i}{M_S} \times \left\{\mathbf{M}_i \times \left[\alpha\mathbf{B}_{\text{Eff}}^i - (\alpha a_{\perp}^i - a_{\parallel}^i)\mathbf{p}_j\right]\right\} \quad (1)$$

where, $\alpha = 0.01$ [39] is the damping constant, γ is the gyromagnetic ratio, $i = 1$ and 2 denotes FL₁ and FL₂, respectively, and \mathbf{M}_i is the magnetization vector of the i^{th} FL. Corresponding, magnetization unit vector \mathbf{m}^i is expressed as $[m_x^i \ m_y^i \ m_z^i]$. \mathbf{p}_j is the unit-vector of the spin-angular momentum acting on the magnetic moments of the i^{th} FL due to j^{th} FL, where $i \neq j$. Hence, \mathbf{p}_j for FL₂ dynamics is parallel to \mathbf{M}_1 , while for FL₁ dynamics its anti-parallel to \mathbf{M}_2 . $M_S = 1.2573 \times 10^6$ A/m [40] is the saturation magnetization of CoFeB based FL, $\mathbf{B}_{\text{Eff}}^i$ is the effective magnetic field acting on i^{th} layer obtained as (superscript i is implied, wherever applicable, in all equations below),

$$\mathbf{B}_{\text{Eff}} = \mathbf{B}_{\text{Applied}} + \mathbf{B}_{\mathbf{K}} + \mathbf{B}_{\text{Dipole}} - \mathbf{B}_{\text{Demag}} + \mathbf{B}_{\mathbf{T}} \quad (2)$$

where, $\mathbf{B}_{\text{Applied}}$ is a external bias magnetic field and set to zero vector in this work, $\mathbf{B}_{\mathbf{K}}$ is uniaxial crystalline anisotropy field obtained as,

$$\mathbf{B}_{\mathbf{K}} = \frac{2}{M_S} \left(K_{\text{Bulk}} + \frac{K_{\text{Interface}}}{t_{\text{FL}}} \right) [0 \ 0 \ m_z]^T \quad (3)$$

where, $K_{\text{Bulk}} = 2.245 \times 10^5$ J-m⁻³ and $K_{\text{Interface}} = 1.286 \times 10^{-3}$ J-m⁻² [40] is bulk and interface anisotropy constant, t_{FL} is the free-layer thickness in meter, $\mathbf{B}_{\text{Dipole}}$ is the dipolar field acting on i^{th} layer due to presence of j^{th} layer and expressed as,

$$\mathbf{B}_{\text{Dipole}}^i = \mu_0 M_S \begin{bmatrix} D_{xx} & D_{xy} & D_{xz} \\ D_{yx} & D_{yy} & D_{yz} \\ D_{zx} & D_{zy} & D_{zz} \end{bmatrix} \begin{bmatrix} m_x^j \\ m_y^j \\ m_z^j \end{bmatrix} \quad (4)$$

where, \mathbf{D} is the 3×3 dipolar-tensor and is calculated directly via analytical expressions from Ref. [41, 42]. $\mathbf{B}_{\text{Demag}}$ is the self-demagnetizing field of the FL, whose vector is expressed as,

$$\mathbf{B}_{\text{Demag}} = \mu_0 M_S \left[N_x m_x \quad N_y m_y \quad N_z m_z \right]^T \quad (5)$$

where, N_x , N_y and N_z is computed via expressions in Ref. [43]. The thermal fluctuation field which induces magnetic noise in both the FLs is computed as [36, 44],

$$\mathbf{B}_T = \sqrt{\frac{2\alpha K_B T}{(1+\alpha^2)\gamma M_S \text{Vol}_{\text{FL}} \Delta t}} \left[R_{0,1}^x \quad R_{0,1}^y \quad R_{0,1}^z \right]^T \quad (6)$$

where, K_B is the Boltzmann constant, Vol_{FL} is the volume of the FL. Along x , y and z -axis, independent random numbers $R_{0,1}$ have Gaussian distribution of zero mean and unit standard deviation. The thermal fluctuation field is accounted at every time-step. Here, we note that the current induced self-heating effects [45-47] have not been included in this work. For high quality MgO MTJs, which lack metallic pinholes in the tunnel junction either due to fabrication process or small cross-section of the MTJ [48], it was experimentally proven [49, 50] that joule heating is not the underlying mechanism for the dielectric breakdown, instead it is the strong electric field larger than 2 V/nm across MgO insulator [49] that result in dielectric breakdown. Since, in this work, we ensure that field is weaker than 1 V/nm and picked high-quality pMTJ [38], these secondary effects are ignored in our analysis. Nevertheless, in case joule heating dominates or is substantial enough to affect the oscillator characteristics, characteristics should in general degrade because of the increase in the magnetic noise and the slight degradation in the spin-polarization of the carriers [51]. Next, MTJ resistance R_{MTJ} calculation accounts for the voltage dependence of the TMR and the dynamic angle θ between the two precessing FLs as,

$$R_{\text{MTJ}} = R_P + \frac{R_{\text{AP0}} - R_P}{1 + \frac{V_{\text{MTJ}}^2}{V_{\text{Half}}^2}} \left(\frac{1 - \cos(\theta)}{2} \right) \quad (7)$$

where, $V_{\text{Half}} = 0.4$ V, extracted for CoFeB from Ref. [52], is voltage across MTJ at which TMR becomes half of its value at zero-bias i.e. $\text{TMR}_0/2$. R_P is the MTJ resistance when both magnets are exactly parallel to each other and remains invariant to V_{MTJ} for all practical purpose [53, 54], while R_{AP0} is MTJ resistance when both magnets are exactly anti-parallel to each other at zero-bias. A pessimistic value of spin-polarization P , $P_1 = P_2 = 0.4$ [55, 56], of the spin-flux for both FLs is assumed to obtain conservative estimates of the oscillator performance. The higher values of P , for instance from 0.5 to 0.8 [51, 55, 56], would proportionally scale down the MTJ current required to obtain the same oscillator frequency. Next, in the recent years Slonczewski expression [57, 58] for spin-torque efficiency η has been extended to account for multiple reflections of the spin-flux [59-61]. Hence, although we have also verified the device operation with Slonczewski expression [58, 62], the results in this article are based on the multi-reflection model and thus the STT efficiency $\eta_{i>j}$ for spin-flux from layer ‘i’ to ‘j’ is computed as [61],

$$\eta_{1>2} = -\eta_{2>1} = \frac{P - P\xi\cos(\theta)}{1 - \xi^2\cos^2(\theta)}, \text{ where } \xi = 1 - 2\varepsilon + 2\varepsilon^2 \text{ and } \varepsilon = \frac{1 - P}{2} \quad (8)$$

Hence, DLT with linear dependence on V_{MTJ} and FLT with the quadratic dependence on V_{MTJ} are respectively obtained as,

$$a^i = \frac{\hbar}{2e} \frac{\eta_{j>i}}{\text{Vol}_{\text{FL}}^i R_{\text{MTJ}}} V_{\text{MTJ}}, \quad a_{\perp}^i = v \frac{\hbar}{2e} \frac{\eta_{j>i}}{\text{Vol}_{\text{FL}}^i R_{\text{MTJ}}} V_{\text{MTJ}}^2 \quad (9)$$

where, e is the electronic charge and $v = 2.97/7.82$ is the ratio between the torques extracted from Ref. [53] (for range of values in literature see Table 2.1 and 2.2 of thesis from Kerstin Bernert [63]).

The voltage-dependent MTJ resistance is coded in verilog-A. The output and transfer characteristics of the high performance NMOS are extracted from the following experimental data from major foundries presented in IEDM (IEEE International Electron Device Meeting) over the years: 130 nm node bulk-NMOS data from Fig.4 and Fig. 6 of Intel transistors

published in Ref. [64], 65 nm node bulk-NMOS data from Fig. 6 and Fig. 7 of IBM, Chartered and Infineon transistors published in Ref. [65], while 14 nm node FinFET (Fin Field Effect Transistor) from Fig. 5 and Fig. 6 of Intel transistors published in Ref. [66]. The channel area for 130 nm and 65 nm is computed as product of channel-length times channel-width, while for 14 nm FinFET its gate length times fin pitch times number of fins (n), where n is an integer not less than the real number obtained by dividing effective channel-width by fin-width (fin-width = 2 fin-height + fin-thickness). The predictive technology files (PTM) available from University of California Berkley (UCB) have been optimized to fit the transistor characteristics. The transistors are modeled via open-source BSIM4 verilog-A code from Silvaco for bulk-NMOS and from UCB for FinFETs. The circuit is simulated via SPICE solver SMASH 6.5.0 from Dolphin Solutions. The fitting (red line) of NMOS output characteristics via spice simulation against the extracted data (black circles) is shown for instance in Fig. 2(c) for 130 nm node, Fig. 2(d) for 65 nm node and Fig. 2(e) for 14 nm node. 65 nm node with $V_{DD} = 1.1$ V, $V_{GS} = 1.1$ V and channel width to length ratio (W/L) = 25 is chosen as a default configuration for NMOS unless specified otherwise.

III. RESULTS and DISCUSSION

A. Operation Principle

Figure 1 illustrates the operation principle of the proposed design. For electron flow along +z-axis, the transmitted spin-flux oriented parallel to \mathbf{M}_1 acts on FL_2 to attempt to align FL_2 parallel to FL_1 , while the reflected spin-flux from FL_2 which is anti-parallel to \mathbf{M}_2 , attempts to align FL_1 anti-parallel to FL_2 . In addition to the STT effect, the z-component of the dipolar-field between both FLs attempts to align them in parallel, while x- and y-components of the dipolar field which participate in dynamics when FLs are not aligned along z-axis attempt to align FLs in anti-parallel configuration. Moreover, these two sets of

contentions, anisotropy field attempts to drive FLs along $+$ or $-z$ -axis depending on if \mathbf{M} is above or below the x - y plane respectively, while demagnetizing field opposes the magnetization vector in respective FLs. For reflected flux to effectuate the switching, FL_1 should be weaker than FL_2 . This implies that the critical current for switching FL_1 as free-layer in the traditional pMTJ STT device should be less than the value that would have been obtained for FL_2 as a free-layer. This criterion for the design implies that FL_1 should have weaker PMA (perpendicular anisotropy), i.e. it should be thicker, than FL_2 . For an operational range of the physical and electronic constraints, the above effects enable complete switching of both the FLs successively despite of a unidirectional current, as illustrated in 3D dynamics of the FLs in Fig. 3(a). This is in contrast to traditional STT devices where switching FL into anti-parallel state with respect to (w.r.t) reference layer necessitates a current reversal. The set of FL_1 and FL_2 periodically move across up-up ($\uparrow\uparrow$), to down-up ($\downarrow\uparrow$), to down-down ($\downarrow\downarrow$) to up-down ($\uparrow\downarrow$) state, where up (\uparrow) and down (\downarrow) refer to magnetization along $+$ or $-z$ -axis, respectively, which results in resistance switching between parallel and anti-parallel state, as illustrated in Fig. 3(b). When FLs are in up-up state, up-spins act on FL_2 but down-spins act on FL_1 . In this case, FL_2 is receiving spins of the same orientation as its magnetization and hence, FL_2 remains unaffected. However, for FL_1 , if the current is above the critical current required to switch FL_1 into anti-parallel state, after a certain incubation delay, FL_1 would start to flip to drive pMTJ towards down-up state. In this state, FL_1 receives the spin-flux oriented along the same direction as \mathbf{M}_1 and hence is unaffected. Nevertheless, this transition dynamically starts to change the spin-vector received by FL_2 which now tries to follow switching of FL_1 to align in parallel with it and attempts to drive pMTJ into a down-down state. At the same time, the reflected spin-vector also changes because of the instantaneous change in \mathbf{M}_2 and attempts to push FL_1 to again drive pMTJ into up-down state. These competing effects in asymmetrically designed FLs ensure that FLs flip

each other in stable self-sustained oscillations. We would like to emphasize that this explanation is somewhat oversimplified to enable conceptual understanding of the operation. As can be gauged from the dynamics in Fig. 3(a), the transient magnetization states would rarely be in clear set of up and down states, and mostly would have a significant x and y components thus empowering the contentious effects of the dipolar-coupling to play a significant role in the dynamics. Therefore, as evident in Fig. 3(b) one FL starts to switch before another FL is fully switched. The FL dynamics is, on the other hand, such that although \mathbf{M}_1 and \mathbf{M}_2 mostly do not simultaneously exactly align with the z-axis, they do achieve exact parallel and anti-parallel states. This enables the design to achieve full resistance swing from R_P to R_{AP} and vice-versa. This design attains theoretical maximum swing, with a constant current input, that can be obtained via STT oscillation, which to the best of our knowledge is not possible even in STNOs with in-plane FL with perpendicular polarizer (pi-Fixed) and perpendicular FL with in-plane reference layer (ip-Fixed) [32, 67-69], indicating a novel concept of obtaining oscillations.

These oscillations in resistance electronically translate to the voltage oscillations across a MTJ as shown in Fig. 3(c). The change in R_{AP} and R_{MTJ} as the voltage across the MTJ changes is taken into account as discussed in the methodology section via eq. (7). FFT of the output V_{MTJ} , as shown in Fig. 3(d), enables us to obtain the fundamental tone f_0 . A 3 dBm line below the peak value subsequently gives half-power frequencies f_1 and f_2 on either side of f_0 , linewidth f_2-f_1 and quality-factor (Q) equals $f_0/(f_1-f_2)$. In Fig. 3(c), an odd observation in this design is the strong amplitude-fluctuations for small V_{MTJ} i.e. when FLs are or nearly parallel to each other. These fluctuations occur because of the strong dipolar coupling between FLs which tends to lock them together. This assisted with net FLT makes one FL precess around another while DLT tries to align them with damping governed by the damping factor α . Increasing α , weakening dipolar field or weakening FLT reduces this noise,

but the oscillator's frequency also reduces. Furthermore, for very high frequency at large currents, i.e. very fast switching, the overlap between dynamics of FL₁ and FL₂ is such that the transient angle between FLs do not reach full 0 and 180 degree, rather the window starts to diminish which degrades the device performance as shown later. To reduce these amplitude-fluctuations, so as to improve the output P_O, would be important for the practical designs implied from these results.

As stated above, there is a physical constraint in pairing of the thickness of the FLs which determines the operability of the design. As a result, Fig. 4 appraises the effect of FL thickness on device operation to show that design can be optimized to meet frequency spectrum for ASICs and IoT LPWAN over a wide range of specifications. To reiterate, for device to work as per our chosen current direction, FL₁ should be weaker (in this case thicker and hence closer to critical thickness at which magnet would become in-plane) than FL₂, so that FL₁ can switch from the reflected spin-flux. As observed from Fig. 4, a smaller difference in the thickness of the two FLs increases the frequency. This, however, reduces the stability of the oscillations such that they die out as the two thicknesses approach each other. As a result, for smaller difference in the thickness, although frequency increases, the tunability via current degrades.

B. Magnetic Noise

Next, we investigate the effect of the thermal fluctuation field that induces a random phase to the magnetization dynamics [70] of both the FLs. Thermal fluctuation field results in a Gaussian noise and modeled by eq. (6) and strongly depends on the volume of the magnet Vol_{FL}. Figure 5 shows that although magnetic noise adversely affects the oscillator performance, the switching based oscillator is much more immune to the thermal field than the precessional orbit-based STNO of similar FL volume. Figure 5(a) shows that both the FLs

still switch and oscillate between $m_z = -1$ and $+1$. Nonetheless, the peak output power P_O drops by -4 dBm in Fig. 5(b) w.r.t peak P_O in Fig. 3(d) without the thermal field. This drop, however, is quite modest compared to what is observed for precessional orbit based STNOs as shown in Fig. 5(c-f). Figure 5(c) and 5(d) illustrate the 3D magnetization dynamics and FFT of V_{MTJ} for an ip-MTJ based STNO of $60\text{nm}\times 40\text{nm}\times 4\text{nm}(1.8\text{nm})$ dimensions, with fixed in-plane pinned layer in place of FL_1 . This device can also be operated without any external bias field and generate oscillations in the microwave range. Magnetic noise strongly afflicts the orbit as shown in Fig. 5(e) which degrades the peak P_O of STNO by -15 dBm in Fig. 5(f) w.r.t peak P_O in Fig. 5(d). The power gets distributed into the adjacent frequencies which broadens the linewidth and degrades the Q . In spintronic oscillators, since magnetic noise afflicts the trajectory of the magnetization vector(s), it affects the dynamic angle between FLs thereby affecting the resistance and subsequently V_{MTJ} oscillations. Therefore, magnetic noise affects both the amplitude-noise and the phase-noise (quality factor) of the spintronic oscillators. Since in this work, switching based design is investigated for only free-running case, we compare with STNO for only free-running case. Injection locking or synchronization of the magnetization dynamics in STNO [14, 15] and phase-locking in ring-oscillators [33] dramatically improves their Q , and may have similar benign effect on the proposed design. This, however, is beyond the scope of the current work and could be a possible future direction to further the investigation of this design. Therefore, for the precessional orbit-based designs (free-running case) scaling down the MTJ dimensions has much worse and stronger effect than on switching based design which thus withstands better chances of down-scaling of the magnets.

C. CCO Configuration

Figure 6 presents oscillator characteristics for representative dimensions of $50\text{nm}\times 50\text{nm}\times 1.6\text{nm}$ (1.2nm) for operation in CCO configuration. In order to focus only on MTJ dynamics, we do not account for the power, area and the design of the current sources/mirrors which would drive these oscillators in sync with STNO literature where it is dealt separately [8, 71]. This issue will be addressed in the next sub-section. In Fig. 6(a), a wide tuning range from 93 MHz to 1002 MHz (red stars) with a tuning ratio of 10.77 is presented. More detailed comparison of the entire performance metrics is given in Table I. It can be found that it is much larger than the values reported for STNOs for current control [32, 67-69] and the ring-oscillators [33]. The output V_{MTJ} (blue circles) roll-down from -27.5 dBm at 93 MHz to -45 dBm at 1002 MHz. As the current increases, the voltage drop across MTJ also increases. This reduces R_{AP} , the maximum resistance of the MTJ for a given operating bias for the anti-parallel state. As a result, the maximum attainable swing for the resistance oscillations decreases as the voltage increases. Therefore, despite of the increase in the current, the V_{MTJ} swing decreases. On the other hand, if there had been no such dependence of the TMR on the voltage bias, the V_{MTJ} swing would have increased. Nevertheless, the effectiveness of the proposed design becomes more evident on computing the power consumed (red stars) and the power efficiency (blue circles), illustrated in Fig. 6(b). With an increasing current, as would be expected, the P_{IN} increases and the efficiency decreases. Efficiency of 0.12%, i.e. nearly -3 on the logarithmic scale, for STNO [32] corresponds to -42 dBm of output, while for the proposed design, at this efficiency, the output is -28 dBm. Finally, Fig. 6(c) demonstrates that due to the increased noise and the amplitude fluctuations at large currents, and hence at higher frequencies, the linewidth (red stars) increases thereby degrading the Q (blue circles). Nevertheless, the observed Q is in the

range of 5.5 to 77.4, which is even better than the Q-factor for free-running STNOs [32]. This again affirms the usefulness of the proposed design.

D. VCO Configuration

D.1. Driven by NMOS

From the practical point of view, for the CCO configuration, the MTJ needs to be driven by a tunable constant current source. Designing a current source in turn would need a few transistors. MTJ is fabricated among higher metal layers as part of BEOL (back-end of line) process while these driving transistors are fabricated during FEOL (front-end of line) process. Therefore, topologically, the transistors are laid out under the MTJ. Hence, the larger of the two areas (MTJ or the driving circuit) gives the actual area occupied by the cell. This indicates that only comparing MTJ area with that of the ring-oscillator to proclaim area advantage for former is not correct. This is an important design consideration often overlooked in spin-oscillator literature. Furthermore, it becomes more difficult to design stable and widely tunable current sources/mirrors, especially at smaller CMOS nodes [8, 71], than designing VCO/CCO with wide tuning range. Therefore, we consider the case of driving MTJ with a single gate-controlled NMOS in this section. Figure 7 illustrates the effect of transition from CCO to gate-controlled VCO configuration. The supply voltage V_{DD} and the gate voltage are fixed whereas the node connecting MTJ with the drain end of the NMOS is floating. The voltage at this node is now the output voltage V_O that would be routed to the subsequent stages driven by the oscillator. Consequently, in VCO configuration we compute P_O corresponding to V_O instead of V_{MTJ} . It is understood that the oscillatory or the AC component of V_O is just inverted w.r.t AC component of the V_{MTJ} , and they are different only w.r.t. DC operating point. As a result, to have a proper comparison of the voltage oscillations between VCO and CCO configuration, V_O in Fig. 7, for a constant current source, is inverted

by subtracting V_{MTJ} from 1.1 V which is the V_{DD} used for the VCO configuration. Figure 7(a, b) show the R_{MTJ} and V_O for CCO configuration for comparison with VCO configuration operating at nearly same frequency (0.7% difference observed in fundamental tone obtained from FFT). To attain this, CCO configuration is operated at the current equal to the average current observed for the VCO configuration. As the resistance of the MTJ oscillates, it changes the quiescent or the DC operating point of the drain end of the NMOS. Therefore, it can be found that not only the voltage across MTJ oscillates but the current through the cell also oscillates, as shown in Fig. 7(c), in anti-phase with R_{MTJ} (Fig. 7(d)) i.e. characteristics of the I_{MTJ} and R_{MTJ} are inverted w.r.t. each other; however, V_O (Fig. 7(e)) oscillates in-phase with the R_{MTJ} . The anti-phase oscillations diminish the output voltage swing. Peak-to-peak voltage swing ΔV can be approximately given by,

$$|\Delta V| \sim |I_{AVG} \cdot \Delta R - R_{AVG} \cdot \Delta I| \quad (10)$$

where, I_{AVG} is the average of the oscillating current I_{MTJ} through the cell, R_{AVG} is the average resistance of the oscillating R_{MTJ} , and ΔI and ΔR are the respective peak-to-peak swings in the current and the resistance oscillations. Equation (10) is mathematically implicit from taking partial derivative of $V_{DS} = V_{DD} - I_{MTJ} \cdot R_{MTJ}$ with proper phase for all three variables. It can be observed that ΔV is not equal to twice of V_O . The magnitude of ΔV includes the amplitude-noise while V_O is the amplitude of the swing over the noise floor. Therefore, V_O cannot be extracted manually from the noisy data, and FFT is performed on the obtained data to estimate V_O . Since, V_O is the actual usable signal, after subtracting for the effect of noise, corresponding usable peak-to-peak value i.e. $2 \cdot V_O$ is smaller than ΔV . Since ΔV can be calculated even manually from simple arithmetic operation on transient plots of I_{MTJ} and R_{MTJ} , and thus more intuitive, it serves as a simple tool to conceptually understand the VCO characteristics, presented in subsequent sub-sections. Equation (10) directly implies that the magnitude of the ΔV (which includes noise) for the proposed oscillator, on being driven in

VCO configuration decreases w.r.t. CCO configuration because ΔI is zero for the later. Consequently, V_O extracted from the noisy data also reduces for the VCO configuration, thereby degrading the output power P_O . Although explicit analysis has not been done for traditional STNO driven by a NMOS like for the proposed design, given the same concept applicable at the drain node for STNO in series with NMOS, we expect similar drop in P_O for STNO case as well in the same configuration.

Another conceptual approach that should assist in understanding the results in subsequent sub-sections is load-line analysis (Fig. 8). Load-line analysis is a standard approach [72] to graphically obtain the DC bias or the quiescent point of the system shown in Fig. 2(a), i.e. it gives the DC current through the NMOS and the DC voltage at the drain terminal. In Fig. 8, for simplicity, R_{MTJ} is treated as a constant i.e. a trivial resistor. As shown in Fig. 8(a), for the gate-control or V_{GS} sweep with fixed V_{DD} , the output characteristics of the NMOS (solid line) i.e. current I_{DS} vs. drain-to-source voltage V_{DS} characteristic for an increasing gate-to-source voltage V_{GS} is intersected with a single dashed line of the output characteristic of a resistor which intercepts the y-axis at V_{DD}/R_{MTJ} and x-axis at V_{DD} , giving a slope of $-1/R_{MTJ}$. The intersections of these two output characteristics are marked via red dots and give the quiescent point or the operating DC conditions. It can be found that as V_{GS} increase, the DC voltage at the drain terminal reduces while the MTJ or the drain current increases. In contrast, for the V_{DD} sweep with a fixed gate voltage, shown in Fig. 8(b), load-line analysis shows a single line (actually superimposed, with larger V_{DD} line overshadowing the smaller V_{DD} trend line) for the NMOS output characteristic, and multiple parallel lines for R_{MTJ} of $-1/R_{MTJ}$ slope, one each for increasing supply voltage V_{DD} . This results in the increase of both the DC voltage at the drain terminal and the drain current when V_{DD} increases. These concepts would be used in section D.2. Next, when both V_{DD} and V_{GS} are fixed in Fig. 8(c) but the resistance of the MTJ is swept, a single line for the NMOS output

characteristic is intersected via respective R_{MTJ} output characteristic line with a corresponding slope. This results in the decrease of both the DC voltage at the drain terminal and the drain current when R_{MTJ} increases. This concept would be useful in understanding [section D.3](#).

D.2. V_{GS} and V_{DD} Control

[Figure 9-11](#) show the control of the oscillator via tuning gate-voltage V_{GS} and node voltage V_{DD} . Although both methods show the same frequency tuning range in [Fig. 9](#), of the two methods, superior characteristics like larger V_O ([Fig. 9](#)) and power efficiency P_O/P_{IN} ([Fig. 10](#)) are exhibited for V_{GS} control of the NMOS, while V_{DD} control exhibits finer linewidth and better quality-factor Q ([Fig. 11](#)). Henceforth, the detailed mechanism behind the observations, their impact on oscillator performance and the trade-offs for controlling via V_{GS} or V_{DD} are expounded in this sub-section.

Impact on Frequency: For both gate and V_{DD} control, the current increases with the voltage which increases the oscillation frequency (see red stars in [Fig. 9](#)). However, it is also observed that frequency linearly increases on tuning V_{DD} , while it saturates for large V_{GS} . This can be understood with the load-line analysis described earlier. In [Fig. 8\(a\)](#), for the gate-control, the quiescent point is in the triode region. As V_{GS} increases, the operational V_{DS} decreases and the I_{DS} increases and both eventually saturate. Conversely, in [Fig. 8\(b\)](#), for V_{DD} control, if the quiescent point (red dots) enter the saturation region of the transistor, the current has almost no change (slightly increase due to non-saturating behavior at smaller nodes due to the short-channel effects), but V_{DS} would continue to increase. If quiescent point is in the triode region, both I_{DS} and V_{DS} would increase continuously. Due to the large R_{MTJ} and relatively large current requirements to switch the FLs, the voltage drop across MTJ forces the transistor to operate in the triode region in this work. Following this operating or the DC bias of the system with NMOS in the triode region, and the current I_{DS} and drain

voltage V_{DS} following the explanation above, the frequency (c.f. Fig. 9; red stars) continuously increases for V_{DD} control while it saturates for the gate-control of the oscillator.

Thereafter, it can be observed that in VCO configuration the lowest frequency operable is lower than that in CCO configuration (see Table I for explicit numbers). At the lowest frequency in the VCO configuration, the average drain current I_{AVG} is lower than the value at which the oscillator works in the CCO configuration. The working of oscillator at such low current can be attributed to the current I_{DS} oscillations in the VCO configuration. During the oscillations, the instantaneous current is much larger than the lowest operating current in the CCO configuration for a substantial fraction of the time-period. This current drive is observed to be still sufficient to trigger the oscillator. At the lowest current drive in the I_{MTJ} oscillation, when MTJ is in the anti-parallel state, the switching dynamics to transition MTJ into a parallel state and thus increase the current drive is sustained mainly via dipolar field.

Impact on Output Power: The downside of the current oscillations in VCO configuration is to degrade the V_O , as discussed earlier and illustrated in Fig. 7. V_O (blue circles in Fig. 9), however, not only degrades but it also exhibits more complex behavior which can be understood via eq. (10). Succinctly, the increasing trend of V_O is observed when the increase in the current outdoes the fall in MTJ resistance due to latter's dependence on the TMR, whereas a decreasing trend of P_O is observed just like for CCO configuration when the increase in the current is insufficient to compensate for the decrease in R_{MTJ} . To obtain the detailed insights, the detailed mechanism is investigated as follows. The current increases as V_{GS} or V_{DD} increases, thus I_{AVG} increase in both cases. Because of the dependence of TMR on V_{MTJ} , the R_{AP} , ΔR and R_{AVG} reduce as the current increase in both cases. The quiescent point of the drain terminal now acts as an additional constraint for regulating potential drop across the MTJ, resulting in constraining of ΔR and R_{AVG} .

Consequently, for V_{DD} control, $\Delta R \cdot I_{AVG}$ first increases and then decreases whereas for gate-control it always decreases and starts to saturate. The non-linear dependence of the current on the respective voltage control and the non-linear relation between R_{MTJ} and the V_{MTJ} results in firstly an increasing and then decreasing trend for ΔI (current oscillations) for the V_{DD} control, whereas it is mainly an increasing trend for the gate-control. With the consideration of R_{AVG} and ΔI together, for both V_{DD} and gate-control, $R_{AVG} \cdot \Delta I$ continuously decreases with an increasing control voltage. Therefore, R_{AVG} , ΔI , ΔR and I_{AVG} collude to result in the change in ΔV with same dependence on V_{GS} and V_{DD} controls as the trends observed for V_O or P_O in Fig. 9. For the results of V_O data, it can be also observed that the gate-control enables larger P_O because of the full-scale V_{DD} which equals to the node supply voltage, but lower V_{DD} due to the V_{DD} -control for the oscillator inherently limits the V_O and the P_O . Conspicuously, irrespective of the control, one shortcoming of this design, compared to a ring-oscillator (see Table I) used for ASIC clocks, is still much lower output power, indicating that an additional amplifier driven by V_O signal may still be needed and consume additional area and energy. The design of this amplifier, however, is beyond the purview of the current work and hence the configurations in Table I for each column are prudently specified to bring out this difference explicitly to notice.

Impact on consumed power and power-efficiency: Next, the power consumed P_{IN} (red stars) in Fig. 10, as expected, follows the same trend as the current or the frequency for respective type of voltage controls. Larger P_O for the gate-control, with P_{IN} in the same range as for V_{DD} -control, evidently results in a larger power-efficiency P_O/P_{IN} (blue circles) for the gate-control. Furthermore, for the gate-control, the cell does not load the preceding driving stage or the circuit which generate the control voltage because of the large (theoretically infinite) input impedance of the gate terminal of the transistor. For the V_{DD} -control, the drain-to-source impedance is much smaller w.r.t. gate input impedance and thus loads the driving

circuit. Therefore, for practical designs, gate-control of the oscillator is suggested instead of the V_{DD} -control method of the ring-oscillators.

Impact on linewidth and quality-factor: The linewidth, and the inferred quality factor, extracted from the FFT, follow even more complex behavior as shown in Fig. 11. In addition to magnetic noise which has Gaussian random distribution, the complexity is enhanced due to the amplitude-noise generated when R_{MTJ} tends to R_P (c.f., Fig. 3(c)). As discussed in the operation mechanism, when the two FLs become nearly parallel, one FL starts to strongly precess around another, resulting in rapid oscillations. These two random factors add to the previous circuit analysis propounded for the frequency and P_O trends. As a result, it is more meaningful to look at the overall trend instead of the exact points for the linewidth and the quality factor in Fig. 11. Overall, it is observed that linewidth (red stars) and quality-factor (blue circles) are best for mid-range control voltage for both V_{DD} and V_{GS} control, and degrade as the voltage is either reduced or increased. As mentioned above in the operation mechanism, at the larger frequencies at the larger currents corresponding to the larger control voltages, the dynamic angle θ between FLs may not reach full 0 and 180 degree and starts to diminish. Alternatively, it can be understood as an increase in the overlap between the transient characteristic of the m_z of the two FLs or the asymmetric phase shift in the transients. In other words, larger currents trigger faster switching of the two FLs which are affected asymmetrically because of their asymmetric design (different thickness for the same ferromagnetic parameters). This not only slightly reduces V_O but also increases the importance of the traditional precessional trajectories and concurrently increases the fraction of time per cycle spent by one FL to precess around another when they are nearly parallel.

For relatively lower currents, the ability to achieve exact parallel and anti-parallel states considerably reduces the torques that act on FLs to destabilize them from the alignment. The increased weightage or the importance of the precession thus increases the

importance or the influence of the magnetic noise on the oscillations, which results in the increased linewidth and the reduced quality factor. On the other hand, as the voltage decreases, the MTJ current reduces and approaches the value of the critical current required for the switching of each FL. This has two key implications. Firstly, as expected, the incubation time for the onset of the oscillations, i.e. triggering the oscillator, increases (not shown). Secondly, the incubation-delay from period-to-period in the oscillations becomes more evident. This happens because the switching is now slow enough to have FLs in perfect parallel and anti-parallel states with both \mathbf{M}_1 and \mathbf{M}_2 aligned along z-axis long enough, rendering the torques to near zero such that the following effects play a significant role. The role of dipolar-field becomes important to unlock from these conditions, especially when the FLs are in anti-parallel configuration. However, more importantly, it is the dependence on the random thermal-field which increases to unlock from these alignments. This becomes the key cause of the period-to-period variations from the oscillations between R_P and R_{AP} states, since the random thermal-fields introduce random angle-offsets in θ making one switching cycle faster than the other. Therefore, the linewidth increases and the quality factor decreases for very weak currents. It can be found that the same physics is also illustrated in [Fig. 6\(c\)](#) for the CCO operation where linewidth increases for the small currents.

Lastly, the Q factor, computed as $f_0/(f_1-f_2)$ i.e. the ratio of fundamental tone to the linewidth, follows the simultaneous effect on the fundamental frequency and the linewidth for both CCO and the VCO configurations. Hence, at both ends of the current strength, the linewidth is large and the quality factor is small. The Q is in the range of 3 to 39.4, which is lower than the values obtained in CCO configuration, but still comparable to the free-running STNOs reported in the range of 8 to 39 [\[32\]](#). The VCO frequency is now in the range of 85 MHz to 420 MHz, which limits its applicability to ASIC clocks, with the tunability ratio of 4.92. This ratio is still much greater than both for STNO and ring-oscillators (see [Table I](#)).

These results show that even in the VCO configuration with a single NMOS, the proposed design can contest with the effectiveness of the other oscillator designs.

D.3. MTJ Area

Figure 12 next appraises the effect of scaling MTJ cross-section for fixed drive strength of the NMOS. As the area of the MTJ is scaled, it proportionately scales the R_{MTJ} because of a constant RA-product. In Fig. 12(a), the oscillator frequency goes down with the increasing area because the current density scale-down almost quadratically with the MTJ dimension. Deviation from the quadratic trend happens because of the changes in the DC bias conditions (see red dots in load-line analysis illustrated in Fig. 8(c)), due to the change in R_{MTJ} . As observed in Fig. 8(c), as the R_{MTJ} scales-down for the fixed operating condition of the NMOS, the drain current and the DC voltage of the drain terminal increases while DC bias across MTJ i.e. approximately the average value of the V_{MTJ} reduces. This increase in the current, however, cannot over-ride the decrease in the current density due to the quadratic effect of the scaling-up of the MTJ dimension. Hence, the frequency (red stars) scales-down but the trend is weaker than the trend that would have been obtained for pure quadratic effect of area scaling. Fixed RA product also results in scaling down of both ΔR and R_{AVG} which is again weaker because of the smaller DC value of V_{MTJ} caused by the shift in the bias conditions. The shifts in the bias conditions also allow for much more steep increase in I_{AVG} than in ΔI . This is further assisted positively by an increased thermal stability of the MTJ because magnetic noise is directly proportional to the square-root of the volume of the magnet. Because of these three reasons, the output power P_O (blue circles) increases with the increasing cross-section but at the cost of the frequency. Increase in the current also results in increase in P_{IN} (red stars) as shown in Fig. 12(b), but the improvement in P_O still results in a higher power-efficiency (blue circles) for the larger MTJ cross-sections. Furthermore, as

expected from the effect of the volume of the magnet on the magnetic noise, the linewidth and the quality factor improve, i.e. linewidth (red stars) reduces and Q (blue circles) increases, as the MTJ cross-section increases in Fig. 12(c). For 40-50%, increase in the dimension from 50 nm to 70-75 nm or nearly twice the increase in the area of the MTJ, Q has increased by nearly three times from 26 to 85. This shows that if for a given frequency the design permits the use of a larger MTJ, it could be extremely advantageous in terms of the output power, power-efficiency and the quality factor. To examine this viability, we next appraise the scaling of the drive strength of the NMOS across three CMOS nodes and understand how they provide the margin for using larger MTJs despite of scaling-down of the CMOS nodes.

D.4. NMOS W/L Scaling

In Fig. 13, the effect of scaling channel width of NMOS to its length, i.e. W/L ratio, for 14 nm (red stars), 65 nm (blue circles) and 130 nm (magenta squares) CMOS node is studied, integrated with MTJ of dimensions $50\text{nm} \times 50\text{nm} \times 1.6\text{nm}$ (1.2nm) i.e. cross-sectional area of $0.0025 \mu\text{m}^2$. As expected the average current I_{AVG} for all three nodes increases with the increasing W/L in Fig. 13(a), and almost saturates because of the integration of the NMOS with the MTJ resistor with determines the DC bias of the system. The channel area is computed based on the approach introduced in the methodology section and illustrated for reference in Fig. 13(b). For 14 nm node, channel-area is from $0.00168 \mu\text{m}^2$ to $0.0468 \mu\text{m}^2$, for 65 nm node it is from $0.009245 \mu\text{m}^2$ to $0.194 \mu\text{m}^2$, and for 130 nm node from $0.0245 \mu\text{m}^2$ to $0.5145 \mu\text{m}^2$ for W/L ratio from 5 to 105, respectively. From Fig. 13(a, c), it is found that for 14 nm node, I_{AVG} is from $168 \mu\text{A}$ at 102.5 MHz to $289 \mu\text{A}$ at 248.5 MHz, for 65 nm node it is from $178 \mu\text{A}$ at 110.12 MHz to $511 \mu\text{A}$ at 518 MHz, and for 130 nm node from $339 \mu\text{A}$ at 292 MHz to $633 \mu\text{A}$ at 656 MHz for W/L ratio from 5 to 105, respectively. The node supply-

voltage V_{DD} is 0.7 V, 1.1 V and 1.3 V, respectively for the three nodes. Hence, it can be observed from the data that MTJ is always smaller than the channel area of the NMOS, except for 14 nm node at $W/L=5$, channel-area for $W/L=10$ at 14 nm node is $0.002646 \mu\text{m}^2$. Furthermore, the channel-area of the NMOS is smaller than the actual area of the NMOS which includes the area for the drain and the source region. This shows that firstly design area would be dominated by the transistor instead of the MTJ and thus should serve as the rightful parameter for comparing area with other designs like ring oscillators. This fact has often being ignored in STNO literature. The power and the area of the driving unit have been ignored as well while comparing the designs. Secondly, within the periphery of the folded (because of the large W/L) NMOS, larger MTJ can be used without any additional penalty on the design area. Therefore, this W/L analysis for the NMOS over three CMOS nodes shows the viability of using larger MTJs to boost the performance of the oscillator. These results also show that MTJ technology does not need to directly scale-down or at least at the same pace with the CMOS technology for the proposed oscillator. Next, the comparison across nodes in Fig. 13(d) shows that using larger nodes for the oscillator design would be beneficial as the nominal supply voltage of the node also scales down with it thereby reducing the drive capability of the transistors. On the other hand, the data also implies that scaling-down the CMOS node limits the operational range of the oscillator and for a given current (iso-frequency) degrades the output and consumes more channel area, for instance compare approximately between the last point of 14 nm and the second point of 65 nm trends.

D.5. Digital Control: DCO Configuration

From the frequency range shown in Fig. 13(c), tunability ratio cannot be computed because channel width is not normally electronically tunable in the VCO or CCO design. This constraint can be circumvented and channel widths can be electronically controlled by

re-configuring VCO into a DCO. Since the W/L analysis shows that a large channel width for bulk-NMOS or a large numbers of fins for FinFETs are required to operate this design, it provides the ability to extend the VCO based analog design to a coarse DCO based digital design, as illustrated in Fig. 14(a). For an N-bit digital control from D_0 to D_{N-1} which corresponds to digital input from 1 to 2^N-1 , the width or the number of fins can be discretized across multiple transistors in parallel (wire-ORed i.e. drain terminal tied together) driving a common MTJ. The effective width of the transistor corresponding to a more significant bit ‘m’ would be twice the width or twice the number of fins of the transistor corresponding to the adjacent less significant bit ‘m-1’. In the DCO design, the gate terminal receives full scale voltage as logic 1 and the transistor is turned-off for logic 0 on receiving 0 V input; hence magnitudes of both its V_{GS} and V_{DD} are fixed. This scheme enables an electronic control of the effective channel width or an effective transistor whose channel-width directly corresponds to the digital input. The lowest digital input of 1 obtained by setting only lowest significant bit to logic 1 and others to logic 0 would correspond to the lowest targeted frequency of the oscillator, while the input 2^N-1 obtained by setting all of the N-bits to logic 1 state would correspond to the largest targeted frequency, where the ratio of the largest to the lowest frequency would give us the tunability ratio for the DCO.

Figure 14(b) shows one such example of a 3-bit coarse DCO for 65 nm CMOS node operating with both V_{DD} and V_{GS} at 1.1 V, with gate input being controlled digitally as either 0 V (bit 0) or 1.1 V (bit 1). The channel width of three transistors W_0 , W_1 and W_2 is respectively designed to be 5 L, 10 L and 20 L, where L is the channel-length. The digital input vector $[D_2 D_1 D_0]$ results in 7 possible digital controls 001, 010, 011, 100, 110 and 111, not counting 000 as it turns-off all transistors and switches off the oscillator. These controls correspond to effective W/L ratio of 5, 10, 15, 20, 25, 30 and 35. This discretizes the frequency trend of Fig. 13(c) (blue circles) into 7 output frequencies from 110 MHz to 459

MHz, with a tuning ratio of 4.17. The DCO output characteristic in Fig. 14(b) is observed to be saturating, which implies non-linearity in the input-to-output mapping of the digital-control-to-frequency over the designed frequency regime, in-line with the behavior of current shown in Fig. 13(a). For a larger degree of linearity, DCO can also be re-designed with largest W/L, corresponding to 2^N-1 input, restricted to be around 20 but it would result in maximum frequency of 394 MHz for the chosen set of NMOS and MTJ parameters.

IV. SUMMARY

We propose a fundamentally new concept of obtaining oscillations with frequencies in VHF and UHF bands. We posit a novel scheme of the spin-torque oscillators which is based on the superior full-switching of the free-layers in contrast to the extant precessional orbit-based schemes. Moreover, it is shown that the free-layers can be reversibly switched without reversing the direction of the current. Oscillator is shown to operate without any external magnetic field and any pinned layer. Absence of the need of a pinning layer may in fact result in a smaller stack height and integration of the oscillator in a lower metallic layers in contrast to a standard MTJs which are pushed to higher layers because of a thick stack-size. The oscillator can operate in the range of 85 MHz to 1002 MHz, with the tuning ratio of 10.76 (CCO) and 4.92 (VCO), output from -26 to -47 dBm. The analysis including the driving NMOS shows that NMOS dominate the design area and the larger nodes would be better for driving the proposed oscillator. Moreover, because of the dominance of the transistor on the area, the scaling constraints on the MTJ can be relatively relaxed, and the oscillator performance can be further improved compared to results generally presented in this work. VCO configuration can furthermore be extended into a digital design and used as a DCO. Table I illustrates some of our exemplar results (second and third column) against other oscillators in the literature. It shows that our design may indeed enable very large

tuning-range, with good Q factor and very small area for a decent output signal and power-efficiency, which is much superior to especially STNO, in the frequency range useful for ASIC clocks and long-range low-power IoT communication via LoRa protocol.

Corresponding Authors

†gauravdce07@gmail.com *elelg@nus.edu.sg

ACKNOWLEDGEMENTS

This work at the National University of Singapore was supported by CRP award no. NRF-CRP12-2013-01 and MOE2013-T2-2-125. We gratefully acknowledge the discussions with Xuanyao Fong, the useful review comments on the manuscript from Kien Trinh Quang and Sachin for helping with Fig. 2.

References

- [1] L. Dai and R. Harjani, Design of High-Performance CMOS Voltage-Controlled Oscillators, Springer US, Boston (2003).
- [2] C.C. Chung, W.S. Su and C.K. Lo, A 0.52/1 V Fast Lock-in ADPLL for Supporting Dynamic Voltage and Frequency Scaling, IEEE Transactions on Very Large Scale Integration (VLSI) Systems 24, 408-412 (2016).
- [3] J.V.D. Tang, D. Kasperkovitz and A.H.M.V. Roermund, High-frequency oscillator design for integrated transceivers, Kluwer Academic Publishers, Boston (2003).
- [4] A. Jha, K. Liao, G. Yeap and K.O. Kenneth, Voltage controlled oscillator area reduction in nano-scale CMOS, in 2014 IEEE Radio Frequency Integrated Circuits Symposium (IEEE, 2014), pp.
- [5] T. Chen *et al.*, Spin-Torque and Spin-Hall Nano-Oscillators, Proceedings of the IEEE 104, 1919-1945 (2016).
- [6] T. Chen *et al.*, Integration of GMR-based spin torque oscillators and CMOS circuitry, Solid-State Electronics 111, 91-99 (2015).
- [7] H.S. Choi *et al.*, Spin nano-oscillator-based wireless communication, Scientific Reports 4, 5486 (2014).
- [8] T. Chen, P. Dürrenfeld, S. Rodriguez, J. Åkerman and A. Rusu, A highly tunable microwave oscillator based on MTJ STO technology, Microwave and Optical Technology Letters 56, 2092-2095 (2014).
- [9] T. Moriyama, G. Finocchio, M. Carpentieri, B. Azzaroni, D.C. Ralph and R.A. Buhrman, Phase locking and frequency doubling in spin-transfer-torque oscillators with two coupled free layers, Physical Review B 86, 060411 (2012).
- [10] X. Zhu and J.G. Zhu, Bias-Field-Free Microwave Oscillator Driven by Perpendicularly Polarized Spin Current, IEEE Transactions on Magnetics 42, 2670-2672 (2006).
- [11] D.E. Nikonov and G.I. Bourianoff, Spin torque oscillator having multiple fixed ferromagnetic layers or multiple free ferromagnetic layers, US 8604886 B2, Intel Corporation (Priority Date Dec 20, 2010)
- [12] H. Ryo *et al.*, Magnetic field angle dependence of out-of-plane precession in spin torque oscillators having an in-plane magnetized free layer and a perpendicularly magnetized reference layer, Applied Physics Express 9, 053006 (2016).
- [13] C.H. Sim, M. Moneck, T. Liew and J.-G. Zhu, Frequency-tunable perpendicular spin torque oscillator, Journal of Applied Physics 111, 07C914 (2012).
- [14] T. Nagasawa, K. Kudo, H. Suto, K. Mizushima and R. Sato, Large-amplitude, narrow-linewidth microwave emission in a dual free-layer MgO spin-torque oscillator, Applied Physics Letters 105, 182406 (2014).

- [15] M. Al-Mahdawi, Y. Toda, Y. Shiokawa and M. Sahashi, Low-nonlinearity spin-torque oscillations driven by ferromagnetic nanocontacts, *Physical Review B* 93, 024408 (2016).
- [16] P.M. Braganca, K. Pi, R. Zakai, J.R. Childress and B.A. Gurney, Zero field high frequency oscillations in dual free layer spin torque oscillators, *Applied Physics Letters* 103, 232407 (2013).
- [17] S. Witold, S. Tomasz, W. Jerzy, R. Günter and D. Sebastiaan van, Zero-Field Spin Torque Oscillator Based on Magnetic Tunnel Junctions with a Tilted CoFeB Free Layer, *Applied Physics Express* 5, 063005 (2012).
- [18] M. Hiroki *et al.*, High Q factor over 3000 due to out-of-plane precession in nano-contact spin-torque oscillator based on magnetic tunnel junctions, *Applied Physics Express* 7, 023003 (2014).
- [19] H. Arai, R. Matsumoto, S. Yuasa and H. Imamura, Spin-Torque Induced Oscillation of a Magnetoresistive Nanopillar with a Conically Magnetized Free Layer and an In-Plane Magnetized Reference Layer, *Journal of the Physical Society of Japan* 85, 063802 (2016).
- [20] L. Bianchini *et al.*, Direct experimental measurement of phase-amplitude coupling in spin torque oscillators, *Applied Physics Letters* 97, 032502 (2010).
- [21] Z. Zeng *et al.*, High-Power Coherent Microwave Emission from Magnetic Tunnel Junction Nano-oscillators with Perpendicular Anisotropy, *ACS Nano* 6, 6115-6121 (2012).
- [22] Nomenclature of the frequency and wavelength bands used in telecommunications, International Telecommunication Union Rec. ITU-R V.431-438 (408/2015) (Retrieved 19 November 2016).
- [23] R. Giordano *et al.*, Performance of a high-frequency synthesizable digitally-controlled oscillator, in 2014 IEEE Nuclear Science Symposium and Medical Imaging Conference (NSS/MIC), pp.
- [24] C. Zhiqing *et al.*, A low spur CMOS phase-locked loop with wide tuning range for CMOS Image Sensor, in 2013 IEEE 10th International Conference on ASIC (ASICON), pp.
- [25] Y. Li, L. Liu, X. Huang, R. Zhang and R. Li, Design and ASIC Implementation of High-Speed DDC, in 2011 Second International Conference on Digital Manufacturing and Automation (ICDMA), pp.
- [26] Z. Zhang, Y. Zhiyi, C. Xu and Z. Xiaoyang, A low power 1.0 GHz VCO in 65nm-CMOS LP-process, in 2011 IEEE 9th International Conference on ASIC (ASICON), pp.
- [27] X. Deng, J. Yang and J. Wu, Low jitter ADPLL insensitive to power supply noise, in 2010 IEEE International Conference on Industrial Technology (ICIT), pp.
- [28] Semtech, LoRaWAN Specification v1.0, (January 2015).
- [29] J. Pet, rvi, K. Mikhaylov, H. M. inen and J. Iinatti, Evaluation of LoRa LPWAN technology for remote health and wellbeing monitoring, in 2016 10th International Symposium on Medical Information and Communication Technology (ISMICT), pp.
- [30] J. So, D. Kim, H. Kim, H. Lee and S. Park, LoRaCloud: LoRa platform on OpenStack, in 2016 IEEE NetSoft Conference and Workshops (NetSoft), pp.
- [31] J.P. Bardyn, T. Melly, O. Seller and N. Sornin, IoT: The era of LPWAN is starting now, in ESSCIRC Conference 2016: 42nd European Solid-State Circuits Conference, pp.
- [32] Z. Zeng *et al.*, Ultralow-current-density and bias-field-free spin-transfer nano-oscillator, *Scientific Reports* 3, 1426 (2013).
- [33] H. Gao, L. Sun, X. Kuang and L. Lou, A low-phase-noise ring oscillator with coarse and fine tuning in a standard CMOS process, *Journal of Semiconductors* 33, 075004 (2012).
- [34] D.V. Berkov and N.L. Gorn, Numerical Simulation of Quasistatic and Dynamic Remagnetization Processes with Special Applications to Thin Films and Nanoparticles, *Handbook of Advanced Magnetic Materials*, Springer US, Boston, 794-880 (2006).
- [35] Z. Li and S. Zhang, Magnetization dynamics with a spin-transfer torque, *Physical Review B* 68, 024404 (2003).
- [36] A. Jaiswal, X. Fong and K. Roy, Comprehensive Scaling Analysis of Current Induced Switching in Magnetic Memories Based on In-Plane and Perpendicular Anisotropies, *IEEE Journal on Emerging and Selected Topics in Circuits and Systems* 6, 120-133 (2016).
- [37] Y. Zhou, H. Zhang, Y. Liu and J. Åkerman, Macrospin and micromagnetic studies of tilted polarizer spin-torque nano-oscillators, *Journal of Applied Physics* 112, 063903 (2012).
- [38] G.S. Kar *et al.*, Co/Ni based p-MTJ stack for sub-20nm high density stand alone and high performance embedded memory application, in 2014 IEEE International Electron Devices Meeting, pp. 19.1.1-19.1.4.
- [39] A.A. Timopheev, R. Sousa, M. Chshiev, L.D. Buda-Prejbeanu and B. Dieny, Respective influence of in-plane and out-of-plane spin-transfer torques in magnetization switching of perpendicular magnetic tunnel junctions, *Physical Review B* 92, 104430 (2015).
- [40] S. Ikeda *et al.*, A perpendicular-anisotropy CoFeB–MgO magnetic tunnel junction, *Nature Materials* 9, 721-724 (2010).
- [41] R. Engel-Herbert and T. Hesjedal, Calculation of the magnetic stray field of a uniaxial magnetic domain, *Journal of Applied Physics* 97, 074504 (2005).
- [42] N. Kani, S.C. Chang, S. Dutta and A. Naeemi, A Model Study of an Error-Free Magnetization Reversal Through Dipolar Coupling in a Two-Magnet System, *IEEE Transactions on Magnetics* 52, 1-12 (2016).

- [43] A. Aharoni, Demagnetizing factors for rectangular ferromagnetic prisms, *Journal of Applied Physics* 83, 3432-3434 (1998).
- [44] K. Roy, S. Bandyopadhyay, J. Atulasimha, K. Munira and A.W. Ghosh, Energy dissipation and switching delay in spin-transfer torque switching of nanomagnets with low-saturation magnetization in the presence of thermal fluctuations, arxiv:1107.0387 (2011).
- [45] H. Keiji *et al.*, Effect of Self-Heating on Time-Dependent Dielectric Breakdown in Ultrathin MgO Magnetic Tunnel Junctions for Spin Torque Transfer Switching Magnetic Random Access Memory, *Japanese Journal of Applied Physics* 49, 04DD15 (2010).
- [46] C. Chul-Min *et al.*, Temperature dependence of reliability characteristics for magnetic tunnel junctions with a thin MgO dielectric film, *Semiconductor Science and Technology* 31, 075004 (2016).
- [47] B. Oliver, G. Tuttle, Q. He, X. Tang and J. Nowak, Two breakdown mechanisms in ultrathin alumina barrier magnetic tunnel junctions, *Journal of Applied Physics* 95, 1315-1322 (2004).
- [48] C. Yoshida, M. Kurasawa, Y.M. Lee, K. Tsunoda, M. Aoki and Y. Sugiyama, A study of dielectric breakdown mechanism in CoFeB/MgO/CoFeB magnetic tunnel junction, in 2009 IEEE International Reliability Physics Symposium, pp. 139-142.
- [49] D.V. Dimitrov, Z. Gao, X. Wang, W. Jung, X. Lou and O.G. Heinonen, Dielectric breakdown of MgO magnetic tunnel junctions, *Applied Physics Letters* 94, 123110 (2009).
- [50] S. Amara-Dababi *et al.*, Charge trapping-detrapping mechanism of barrier breakdown in MgO magnetic tunnel junctions, *Applied Physics Letters* 99, 083501 (2011).
- [51] Y. Lu *et al.*, Spin-Polarized Inelastic Tunneling through Insulating Barriers, *Physical Review Letters* 102, 176801 (2009).
- [52] Z. Kugler, V. Drewello, M. Schäfers, J. Schmalhorst, G. Reiss and A. Thomas, Temperature and bias voltage dependence of Co/Pd multilayer-based magnetic tunnel junctions with perpendicular magnetic anisotropy, *Journal of Magnetism and Magnetic Materials* 323, 198-201 (2011).
- [53] H. Kubota *et al.*, Quantitative measurement of voltage dependence of spin-transfer torque in MgO-based magnetic tunnel junctions, *Nature Physics* 4, 37-41 (2008).
- [54] J.C. Sankey, Y.-T. Cui, J.Z. Sun, J.C. Slonczewski, R.A. Buhrman and D.C. Ralph, Measurement of the spin-transfer-torque vector in magnetic tunnel junctions, *Nature Physics* 4, 67-71 (2008).
- [55] K. Takahide, D. Tadaomi, O. Mikihiko, A. Yasuo and M. Terunobu, Tunneling Spin Polarization and Magnetic Properties of Co-Fe-B Alloys and Their Dependence on Boron Content, *Japanese Journal of Applied Physics* 46, L250 (2007).
- [56] S.X. Huang, T.Y. Chen and C.L. Chien, Spin polarization of amorphous CoFeB determined by point-contact Andreev reflection, *Applied Physics Letters* 92, 242509 (2008).
- [57] J.C. Slonczewski, Current-driven excitation of magnetic multilayers, *Journal of Magnetism and Magnetic Materials* 159, L1-L7 (1996).
- [58] J.C. Slonczewski, Currents, torques, and polarization factors in magnetic tunnel junctions, *Physical Review B* 71, 024411 (2005).
- [59] X. Waintal, E.B. Myers, P.W. Brouwer and D.C. Ralph, Role of spin-dependent interface scattering in generating current-induced torques in magnetic multilayers, *Physical Review B* 62, 12317-12327 (2000).
- [60] S. Hernández and R.H. Victora, Calculation of spin transfer torque in partially polarized spin valves including multiple reflections, *Applied Physics Letters* 97, 062506 (2010).
- [61] W. Zhu, Z. Zhang, J. Zhang and Y. Liu, Multiple Reflection Effect on Spin-Transfer Torque Dynamics in Spin Valves with a Single or Dual Polarizer, *SPIN* 05, 1550003 (2015).
- [62] T. Tomohiro, A. Hiroko, T. Sumito, T. Shingo, K. Hitoshi and I. Hiroshi, Critical Field of Spin Torque Oscillator with Perpendicularly Magnetized Free Layer, *Applied Physics Express* 6, 123003 (2013).
- [63] K. Bernert, Spin-transfer torques in MgO-based magnetic tunnel junctions, Doctoral Thesis, Technische Universität Dresden (2014).
- [64] S. Tyagi *et al.*, A 130 nm generation logic technology featuring 70 nm transistors, dual Vt transistors and 6 layers of Cu interconnects, in Proceedings of the International Electron Devices Meeting (IEDM) 2000, pp. 567-570.
- [65] Z. Luo *et al.*, High performance and low power transistors integrated in 65nm bulk CMOS technology, in Proceedings of the International Electron Devices Meeting (IEDM) 2004, pp. 661-664.
- [66] S. Natarajan *et al.*, A 14nm Logic Technology Featuring 2nd-Generation FinFET , Air-Gapped Interconnects, Self-Aligned Double Patterning and a 0.0588 m² SRAM cell size, in Proceedings of the International Electron Devices Meeting (IEDM) 2014, pp. 3.7.1-3.7.3.
- [67] D. Houssameddine *et al.*, Spin-torque oscillator using a perpendicular polarizer and a planar free layer, *Nature Materials* 6, 447-453 (2007).
- [68] O. Boulle *et al.*, Shaped angular dependence of the spin-transfer torque and microwave generation without magnetic field, *Nature Physics* 3, 492-497 (2007).

- [69] F. Ciarán *et al.*, Zero-field spin-transfer oscillators combining in-plane and out-of-plane magnetized layers, *Applied Physics Express* 7, 043001 (2014).
- [70] W.F. Brown, Thermal Fluctuations of a Single-Domain Particle, *Physical Review* 130, 1677-1686 (1963).
- [71] T. Chen, Wideband amplifier design for STO technology, Master's thesis, KTH Royal Institute of Technology (2011).
- [72] A.S. Sedra and K.C. Smith, *Microelectronic Circuits*, Oxford University Press, New York (2004).

Figures

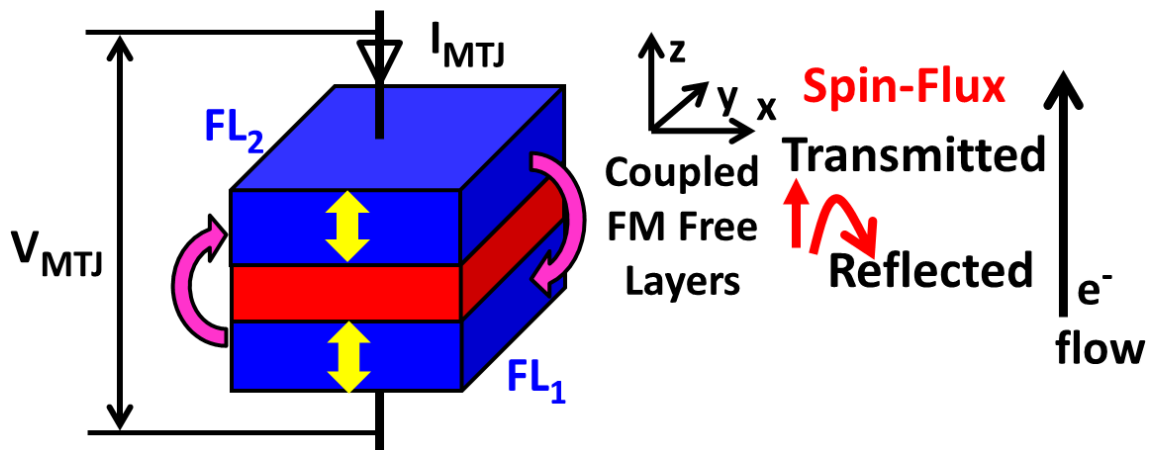


Figure 1. Conceptual illustration of a pMTJ with a dipolar coupled dual free-layer, without any pinned layer. It is driven by a uni-directional current from FL₂ to FL₁. The transmitted spin-flux with vector parallel to the magnetization of FL₁ acts on FL₂, while reflected spin-flux with vector anti-parallel to magnetization of FL₂ acts on FL₁, which for a set of electronic and geometric constraints results in a self-sustained switching of both the free layers producing AC oscillations for a DC bias. When this pMTJ is driven via tunable DC current source I_{MTJ} , the device is in CCO configuration.

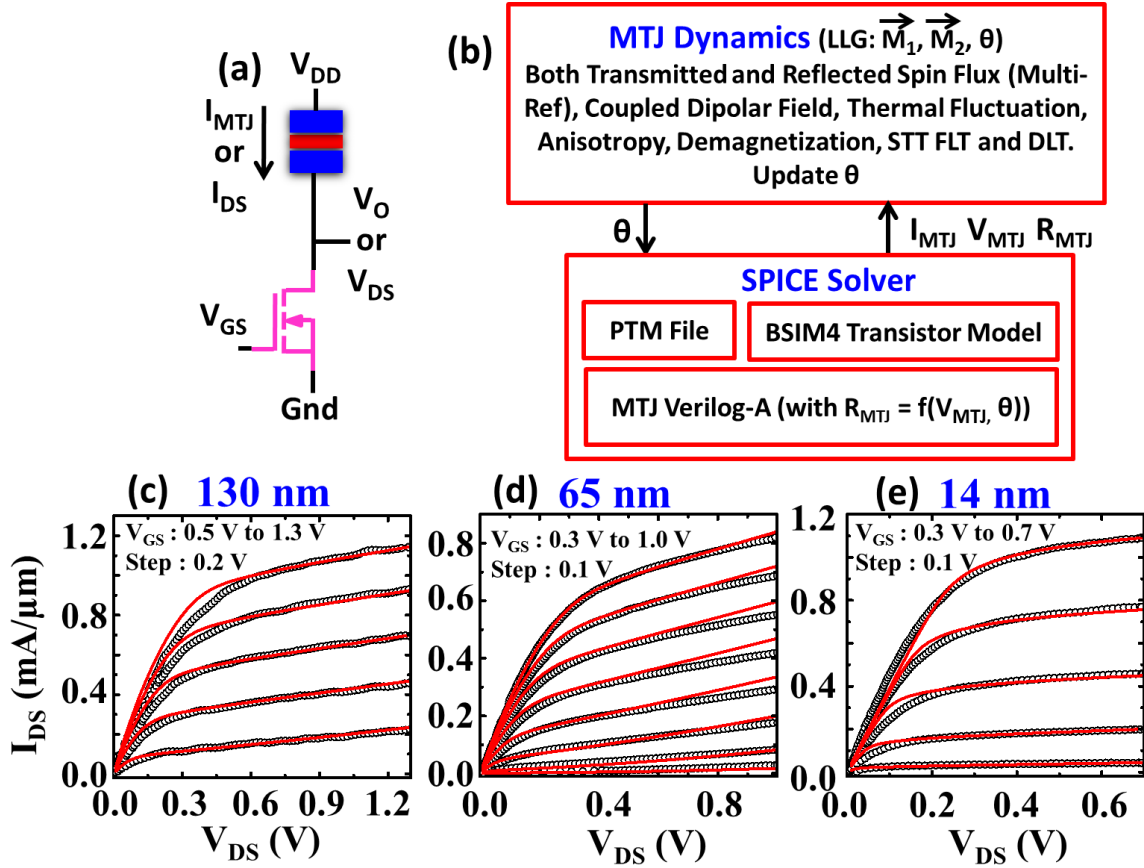


Figure 2. (a) VCO configuration with pMTJ driven via tunable DC V_{GS} for a fixed V_{DD} (gate-control) or tunable DC V_{DD} for a fixed V_{GS} (drain-control). (b) Schematic summary of simulation framework expounded in the methodology section. (c-e) Published experimental data (black circles) of NMOS output characteristics fitted (red line) against BSIM4 model used in spice solver for three representative CMOS nodes. For (c) 130 nm node fitting against Fig. 4 of Ref. [64] from Intel, (d) 65 nm node fitting against Fig. 6 of Ref. [65] from IBM, Chartered and Infineon, and (e) 14 nm node fitting against Fig. 5 of Ref. [66] from Intel.

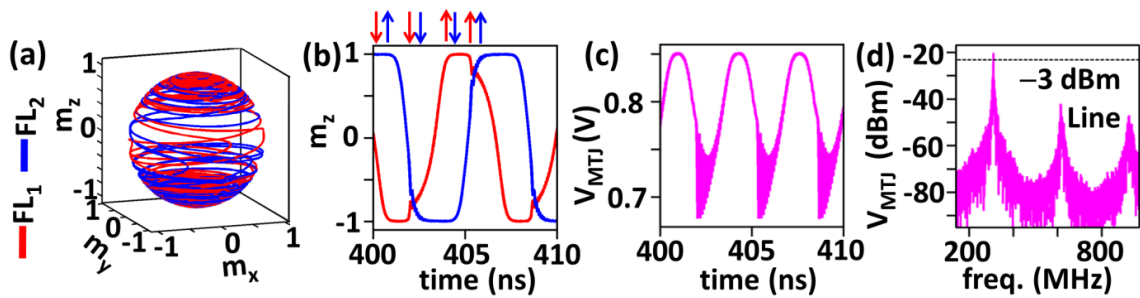


Figure 3. Operation principle (without thermal field) for $50\text{nm} \times 50\text{nm} \times 1.6\text{nm}$ (1.2nm) pMTJ device driven with constant current I_0 of $360 \mu\text{A}$. (a) Dynamics of magnetization unit vector $\mathbf{m} = [m_x \ m_y \ m_z]^T$. (b) Full-switching of both m_z . (c) Output voltage oscillations V_{MTJ} and (d) FFT of V_{MTJ} demonstrating fundamental tone and the harmonics along with -3dBm line used to determine the linewidth of the oscillator.

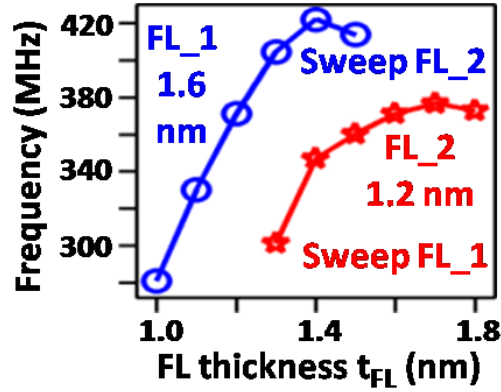


Figure 4. Effect of FL thickness (without thermal field) on the oscillation frequency for a representative I_0 of 410 μ A. MTJ can thus be designed to meet frequency specifications of an oscillator over a wide frequency range.

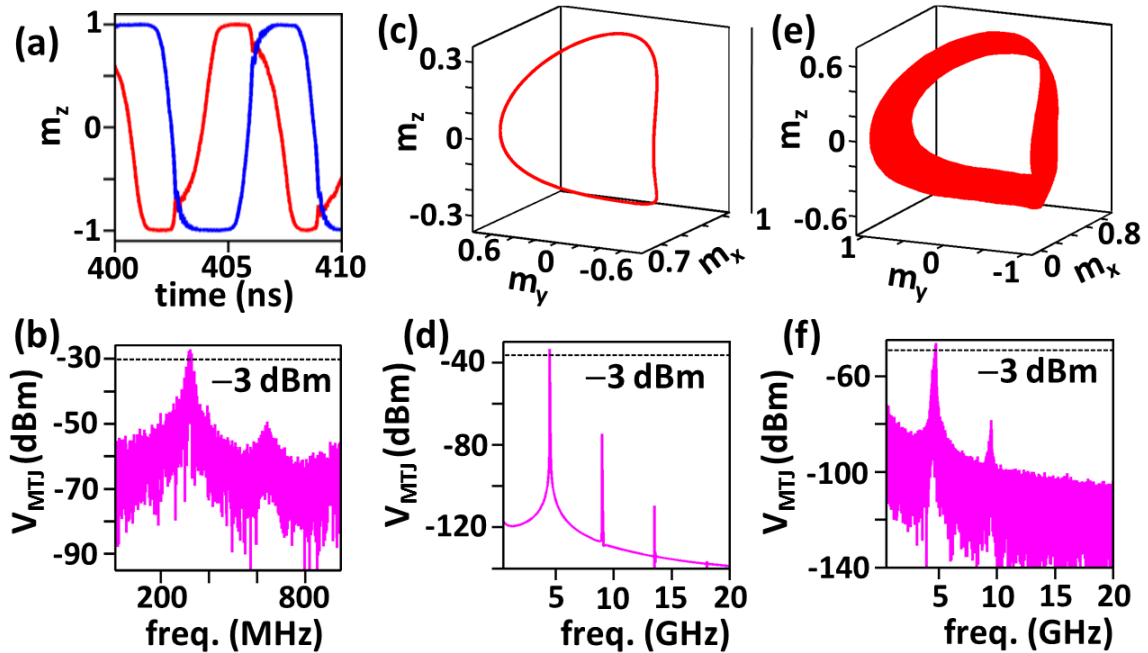


Figure 5. Effect of the thermal fluctuation field or magnetic noise (300 K) on the proposed oscillator (a, b) is contrasted with an orthogonal STNO (c-f), of same RA-product, of 60nm \times 40nm \times 4nm(1.8nm) with in-plane fixed layer (in place of FL₁) and perpendicular free layer (in place of FL₂) operating at 4.5 GHz with 70 μ A fixed current without external bias field. (c, d) STNO without thermal field clearly shows the precessional orbit (c) and FFT of the voltage across MTJ (d). (e-f) STNO with thermal field shows randomness introduced in the orbit ((e) illustration represents only 50 ns of precession), and the linewidth broadening in FFT in (f). Proposed design is shown to be robust to thermal field with minor effect (-4 dBm; calculated between peak V_{MTIJ} in (b) and Fig. 3(d) for fundamental tone) on output and increase in the linewidth, while STNO of comparable cross-section and FL thickness shows strong degradation (-15 dBm; calculated between peak V_{MTIJ} in (f) and (d) for fundamental tone) of output and phenomenal change in the linewidth.

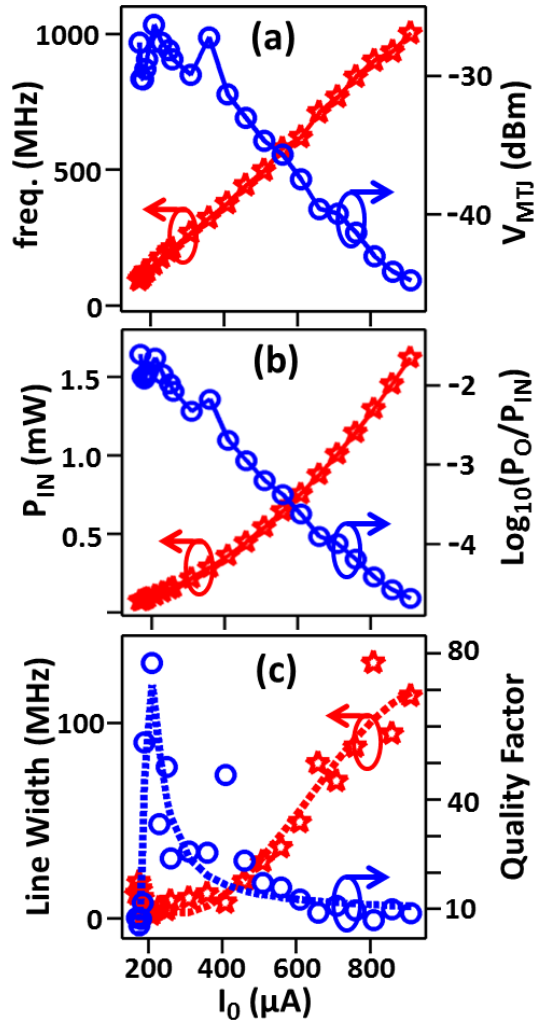


Figure 6. Effect of constant current I_0 on (a) frequency and output voltage oscillations, (b) input power consumed P_{IN} and the power efficiency (P_O/P_{IN}) i.e. delivered output power to the consumed power, (c) linewidth and the quality factor (Q) of the oscillator. Dashed lines are the fit to the data to exhibit an overall trend. (b) Consumed power decreases directly with the current thereby improving the power efficiency especially at the lower frequencies. (c) Frequency spectra narrows at the smaller currents (frequencies) thereby improving the quality factor from 10 to nearly 30.

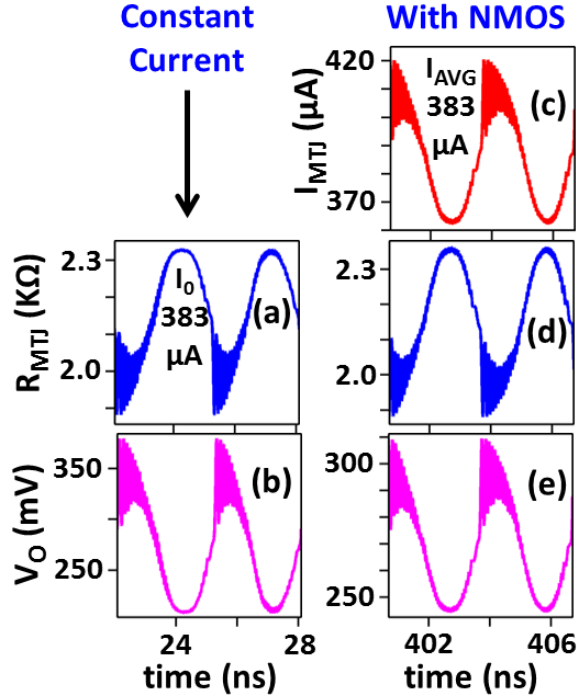


Figure 7. Effect of replacing (a, b) constant current drive with (c-e) NMOS ($W/L=15$) to drive MTJ. For (b) $V_O = 1.1 - V_{MTJ}$ for appropriate comparison with (e). With NMOS, drain current also oscillates in anti-phase with resistance, thereby reducing the output swing which is approximately given by eq. (10). I_0 is chosen equal to the average drain current, and complementary MTJ voltage is used as V_O for constant current case, for rightful comparison.

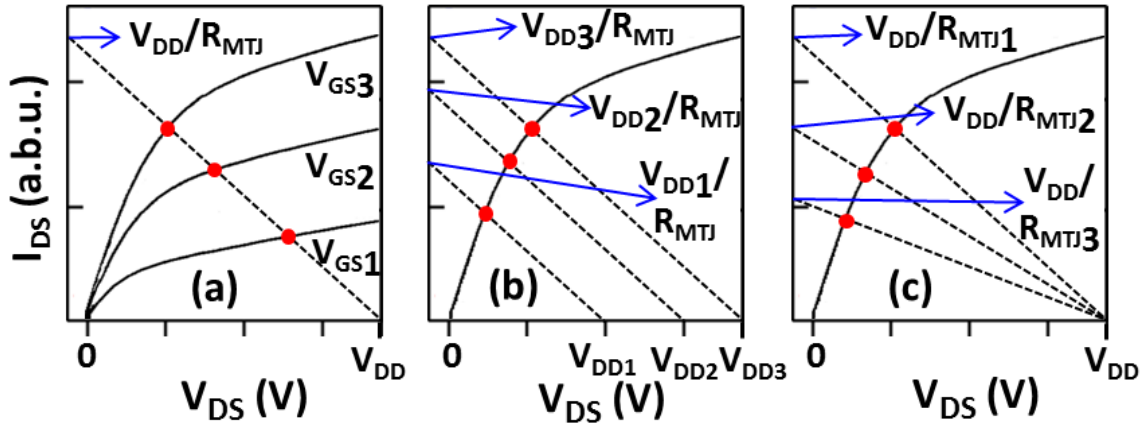


Figure 8. Conceptual illustration of load-line analysis to show the effect of sweeping (a) V_{GS} , (b) V_{DD} and (c) MTJ cross-section. Larger index in the subscript represents a larger magnitude of the corresponding quantity. Solid black line is NMOS output characteristics. Dashed black line is R_{MTJ} output characteristic, where R_{MTJ} is treated as a constant trivial resistor in this illustration. Quiescent point is marked via red dot at the point of intersection of R_{MTJ} and NMOS characteristics. This serves as a visual aid in understanding data for the effect of respective parameters shown in the subsequent figures.

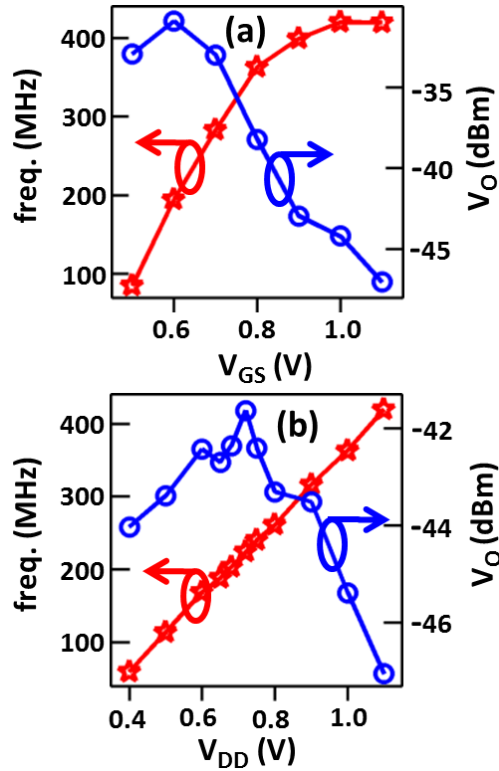


Figure 9. Effect of sweeping (a) gate voltage V_{GS} and (b) node voltage V_{DD} on frequency and output voltage V_O .

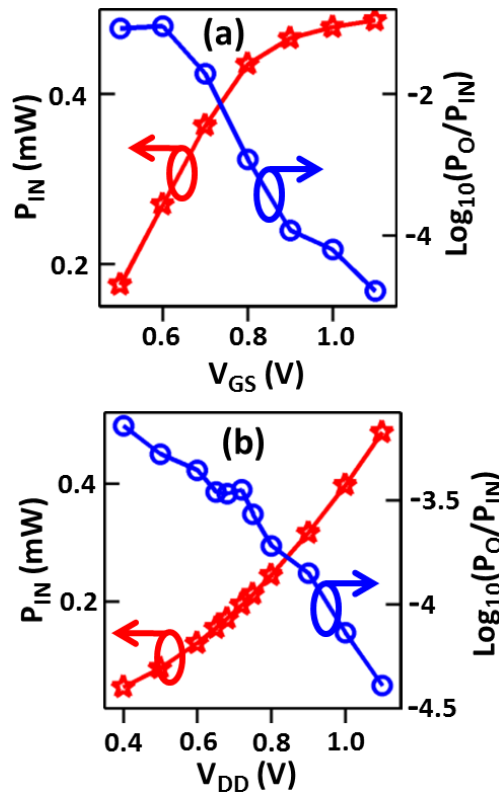


Figure 10. Effect of sweeping (a) gate voltage V_{GS} and (b) node voltage V_{DD} on consumed input power P_{IN} and power efficiency P_O/P_{IN} .

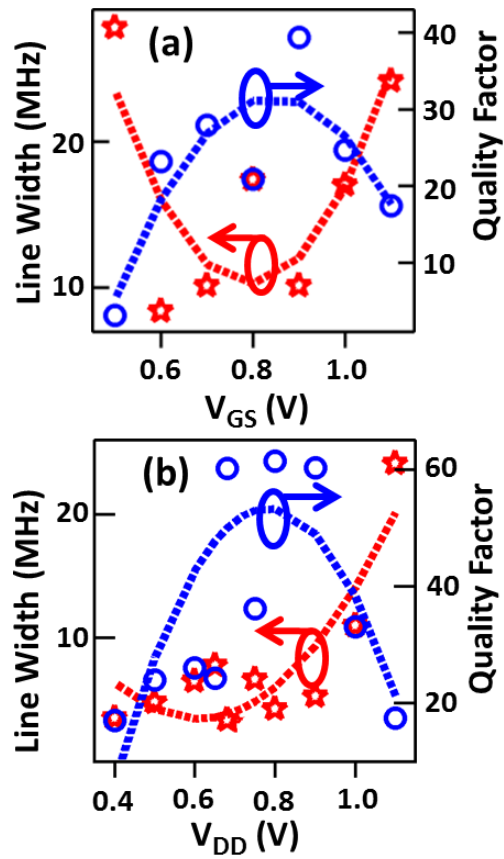


Figure 11. Effect of sweeping (a) gate voltage V_{GS} and (b) node voltage V_{DD} on Linewidth and quality factor Q . Dashed lines in (c, d) are the fit to the data to exhibit an overall trend.

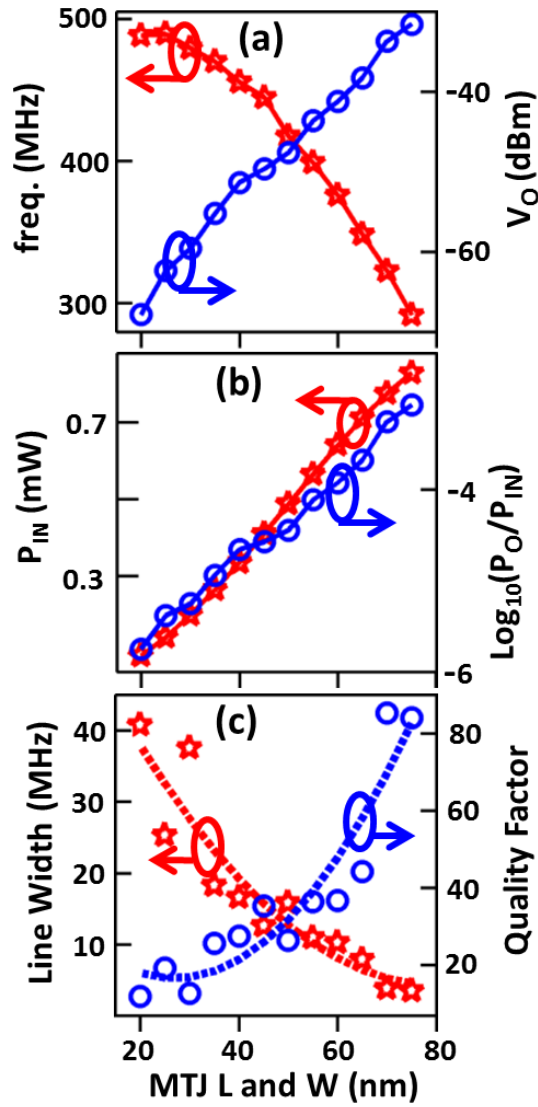


Figure 12. Effect of sweeping MTJ cross-section (length=width) on (a) frequency and output voltage V_O , (b) input power P_{IN} and power efficiency P_O/P_{IN} , and (c) Linewidth and quality factor Q . Dashed lines in (c) are the fit to the data to exhibit an overall trend.

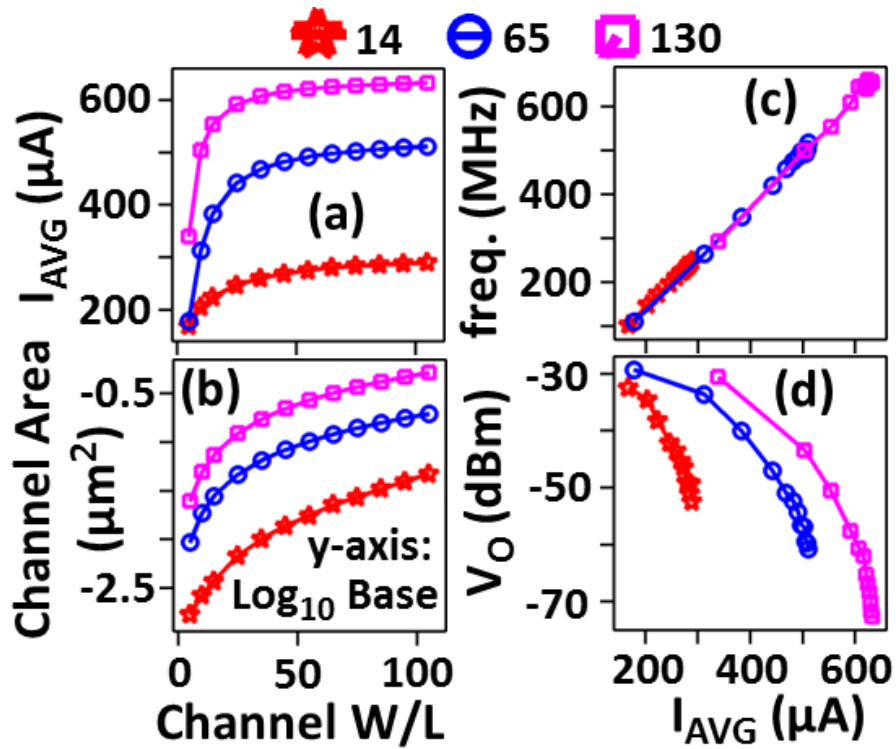


Figure 13. Effect of W/L of transistors on performance across 14 nm, 65 nm and 130 nm node operating at full scale node voltage (0.7, 1.1, 1.3 V) i.e. $V_{DD}=V_{GS}$. (a) Average operating current for the oscillator. (b) Channel area for the reference. Output frequency (c) and the signal amplitude (d).

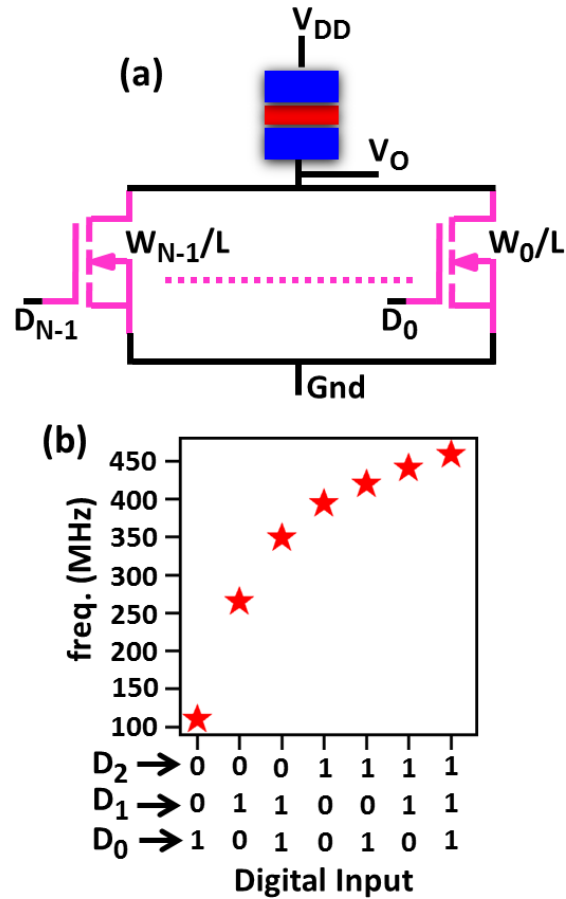


Figure 14. (a) Re-designing VCO into a DCO configuration by splitting the effective transistor width across wire-ORed N -transistors, driven by N -bit digital control D_0 to D_{N-1} . Effective width for bulk-NMOS or number of fins for FinFET of transistor ‘ m ’, driven by bit D_m , is twice the width or number of fins of transistor ‘ $m-1$ ’ where $m \in [1, N-1]$. (b) Frequency obtained for a 3-bit DCO with channel widths of $W_2 = 2 W_1 = 4 W_0 = 20 L$, with a tuning ratio of 4.17.

Table I. Summary of a comparison with other designs in the literature.

Criteria	pp ϑ (C)	pp ϑ, β (NMOS)	STNO κ, χ, δ (pi/ip) (C)	Ring λ, ζ [33]
Freq. (f) (MHz)	93 – 1002	85 - 420	600 – 4000 [32, 67-69]	480-1100
f_{\max}/f_{\min}	10.77	4.92	~ 2 &	1.25
V_O (dBm)	-26 to -45	-31 to -47	-42 &	-2.97
P_O/P_{IN} (%)	2.5 to 0.002	0.3 to 0.004	0.12 &	13.1
Q	5.5 - 77.4	3 – 39.4	8-39 &	-120 to -108 dBc/Hz Φ
Area (μm^2)	0.0025 *	0.0462 #	0.0105 *&	14784 Ψ

C: Driven by Current Source; * MTJ area; # Channel Area; Ψ Core Area;

ϑ . $50 \times 50 \times 1.6(1.2)$; β . Gate Control 65 Node $W/L=25$; δ . $50 \times 40 \times t_1(t_2)$; κ . ii and pp need external B-Field to precesses. χ . TMR Based without additional locking or post-processing circuit; δ See Table 1 of Ref. [32]; & Best of the results of Ref. [32]; λ LC is not compared, because in sub-GHz range on-chip inductor and capacitor size is in hundreds of μm^2 . Its comparison is better suited in high GHz range. Φ Phase Noise (not Q); ζ with PLL lock (not for free-running case).